



Thermal effect of high-power laser propagation in complex channels and its mitigation

XUNQING HUANG,^{1,2} FEI XU,^{1,2} XIANGZHENG CHENG,³
AND SHUAI SHAO^{1,*}

¹Changchun Institute of Optics, Fine Mechanics and Physics, Chinese Academy of Sciences, Changchun 130033, China

²University of Chinese Academy of Sciences, Beijing 100049, China

³Key Laboratory of Electro-Optical Countermeasures Test & Evaluation Technology, Luoyang 471000, China

*sshuaiciomp2021@163.com

Abstract: We investigate the channel thermal effect resulting from the gas thermal blooming effect and mirror thermal deformation on the beam quality, and we propose a mitigation measure for blowing purge gases. Without gas blowing, the gas thermal blooming effect opposes the influence of mirror thermal deformation on the beam phase, resulting in significant phase distortion and offset. Noticeable distortion and divergence of the laser spot was also observed. After blowing purge gases, the beam phase was primarily determined by the mirror thermal deformation. Simultaneously, the mean-squared beam width decreased uniformly, improving the symmetry and energy concentration of the laser spot. However, the laser spot tended to stabilize when the gas velocity exceeded a certain threshold.

© 2023 Optica Publishing Group under the terms of the [Optica Open Access Publishing Agreement](#)

1. Introduction

High-power lasers are extensively utilized in national defense and manufacturing industries because of their excellent directivity, high energy output, and rapid response speed [1–3]. To achieve precise tracking and targeting of the laser on a designated object, the laser beam must traverse a complex channel that can rotate and change the propagation direction multiple times. During this process, the gas medium in the channel absorbs a portion of the laser energy, leading to a local temperature rise and subsequent change in the refractive index, resulting in the gas thermal blooming effect. Simultaneously, mirror thermal deformation also affects the beam quality [4–6]. As the applied laser energy increases, the thermal effect of laser propagation in complex channels exerts a more pronounced destructive influence on the beam, significantly impeding the advancement and practical application of high-power lasers.

The thermal effect of laser propagation has been a focus of continuous research in recent decades. Gebhardt and Smith developed a theoretical model to predict the steady-state self-induced thermal distortion of a laser beam in an absorbing medium along the transverse direction of propagation [7]. They also reviewed the development of thermal blooming along the 25 years before 1990 [8]. Fleck *et al.* described the calculation of the time-dependent three-space-dimensional laser beam propagation. These methods are applicable to the propagation of high-energy laser beams through gases in the presence of horizontal wind and turbulence [9,10]. Researchers have developed numerical models to analyze the thermal blooming effect of different types of laser beams, including Gaussian, Airy, Hermite-Gaussian, vortex, and array beams, propagating in the atmosphere. These models were used to investigate the gas thermal blooming effect on the laser beam quality under different parameters and provide detailed explanations of the changes in the intensity distribution, centroid position, and mean-squared beam width of laser beams propagating through a medium [11–17]. The thermal blooming effect of high-power laser propagation in rain and sea environments was also analyzed using a numerical simulation method [18–20]. Lu

et al. proposed a feasible approach to obtain the phase change induced by thermal blooming. Additionally, based on the phase change, an alternative solution for phase compensation near the receiver was provided [21]. Due to the movement of the propagation medium, a high-power laser cannot produce a stable thermal blooming effect. Spencer used wave-optics simulations to examine Monte Carlo averages associated with turbulence and thermal blooming (steady-state, time-dependent) with the goal of investigating turbulent thermal blooming interactions [22,23]. The principle of analyzing the thermal effect of high-power laser propagation over short distances in complex channels is similar to that of long-distance atmospheric propagation. However, analyzing the thermal effect in a channel is a more complex and comprehensive problem. The main factors affecting the thermal effect of the channel are as follows. First, the channel includes the thermal blooming effect caused by the gas and thermal deformation of the mirror. Second, the temperature rise in the gas and mirror differs when they absorb laser energy and heat is transferred between them. Third, the temperature in the channel increased, but failed to dissipate heat promptly, leading to irregular heat accumulation. The fourth is the interaction between the turbulent gas motion and thermal effect of the channel after blowing the purge gas.

This study provides a comprehensive analysis of the thermal effects of high-power laser propagation through complex channels. Additionally, a mitigation measure involving the use of a blowing purge gas was proposed, and an in-depth analysis and a comparison of the changes in beam quality after the blowing process were conducted. Section 2 provides a theoretical description of the channel thermal effect resulting from the gas–thermal blooming effect and mirror thermal deformation. In Section 3, a numerical model is established to describe the thermal effects of the channel. In this section, we analyze and compare the variation characteristics of the channel temperature distribution, beam phase, and laser spot parameters (centroid position, mean-squared beam width, and energy Strehl ratio) with the laser propagation time and power, while considering the presence and absence of purge gas blowing. Additionally, the mitigation effect of different gas velocities on the channel thermal effect was examined. In Section 4, an experimental platform for the simplified channel is constructed, and a comparison is made between the experimental and simulation results regarding the distribution characteristics of the beam phase difference. Section 5 summarizes the results of this study.

2. Theoretical model

It was assumed that the high-power laser propagated along the z -axis of the channel. Under the paraxial approximation, Maxwell's wave equation is expressed as follows [9,10]:

$$2ik \frac{\partial E}{\partial z} = \nabla_{\perp}^2 E + k^2 \left(\frac{n^2}{n_0^2} - 1 \right) E, \quad (1)$$

where E is the envelope of the electric field, the wavenumber related to the wavelength is $k = 2\pi/\lambda$, $\nabla_{\perp}^2 = \partial^2/\partial x^2 + \partial^2/\partial y^2$ is the transverse Laplace operator, n_0 is the refractive index before perturbation, and n is the refractive index after perturbation.

Let E^n be the complete solution to Eq. (1) at $z = z^n$. The solution at $z = z^{n+1}$ may be written as follows [9,10]:

$$E^{n+1} = \exp\left(-\frac{i}{4k} \Delta z \nabla_{\perp}^2\right) \exp\left[-\frac{ik}{2} \int_{z^n}^{z^n+\Delta z} \left(\frac{n^2}{n_0^2} - 1\right) dz\right] \exp\left(-\frac{i}{4k} \Delta z \nabla_{\perp}^2\right) E^n, \quad (2)$$

Equation (2) shows that propagation over distance Δz comprises vacuum propagation of the field over distance $\Delta z/2$, an increment of the phase in accordance with nonlinear medium changes, followed by vacuum propagation of the resulting field over distance $\Delta z/2$.

The laser output was assumed to have a Gaussian distribution for a continuous laser beam. After the laser beam passes through the beam expander-collimator system, the optical field

distribution at the initial plane ($z = 0$) can be expressed as follows:

$$E(x, y, z = 0) = \sqrt{\frac{2P}{\pi\omega_0^2}} \exp\left(-\frac{x^2 + y^2}{\omega_0^2}\right), \quad (3)$$

where P is the laser power and ω_0 is the beam waist radius.

The laser beam intensity distribution of a beam propagating in a gas medium can be expressed as follows:

$$I = |E|^2 \exp(-\alpha_1 z), \quad (4)$$

where α_1 is the absorption coefficient of the gas medium.

Under isobaric conditions, the hydrodynamic equation describing the change in gas density in the time-dependent thermal blooming problem can be expressed as follows:

$$\frac{\partial \rho_1}{\partial t} + \mathbf{v} \cdot \nabla \rho_1 = -\frac{(\gamma - 1)}{c_s^2} (\alpha_1 I + Q_1), \quad (5)$$

where c_s represents the speed of sound, γ denotes the specific heat ratio, ρ_1 represents the change in gas density, and Q_1 denotes the heat transferred by the mirror to a unit volume of gas per unit time.

The relationship between the refractive-index fluctuations and gas density in the channel can be expressed by the following structural equation [24]:

$$\frac{n - n_0}{n_0 - 1} = \frac{\rho_1}{\rho_0}, \quad (6)$$

where ρ_0 is the density of the gas with no perturbations.

During laser propagation in the channel, the change in the refractive index of the gas is determined by the change in its density. At time t , let the gas refractive index of the cross section at $z = z_1$ be n_1 and the gas refractive index of the cross section at $z = z_1 + \Delta z$ be n_2 . When Δz is sufficiently small, the phase difference $\Delta\phi_1$ between the two cross-sections can be expressed as follows:

$$\Delta\phi_1 = k \int_{z_1}^{z_1 + \Delta z} \Delta n dz \approx k \left(\frac{n_1 + n_2}{2} - n_0 \right) \Delta z. \quad (7)$$

After the laser passes through the gas medium, the intensity distribution on the mirror surface is assumed to be I_1 . Figure 1 shows the structure and boundary conditions of the mirror. It can be observed that the mirror comprises a monocrystalline silicon substrate and a gold film, and the surface of the film is exposed to a gas environment. The interface between the gold film and gas is S_1 , and the interface between the silicon substrate and gold film is S_2 . In addition to S_2 , the remaining surfaces of the monocrystalline silicon substrate were considered to be adiabatic. The mirror temperature increased with the absorption of a portion of the laser energy. At time t , T_0 represents the temperature field distribution of the gas in proximity to the gold film, T_g denotes the temperature field distribution of the gold film, and T_s represents the temperature field distribution of the silicon substrate.

In order to simplify the calculation model, the scattering on the gold film is neglected. The gold film has an extremely high absorption coefficient, and it is assumed that the gold film receives all the energy absorbed by the mirror, and heat exchange occurs between the gold film and gas. Assuming that the gold film is thin, the temperature of interface S_2 is considered to be equal to that of the gold film T_g . Consequently, the energy absorbed by the gold film leads to temperature rise and thermal deformation of the silicon substrate through heat conduction. It is assumed that the gold film and monocrystalline silicon substrate are isotropic, and their

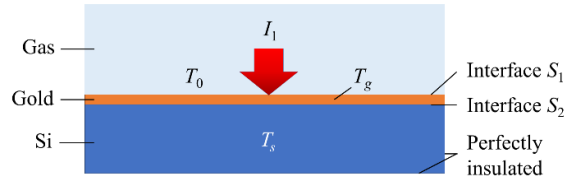


Fig. 1. Structure and boundary conditions of the mirror.

thermophysical parameters are constant. The temperature distribution of the gold film and silicon substrate can be described by the heat conduction equation as follows [25]:

$$\nabla \cdot \kappa \nabla T + Q_2 = \rho c_p \frac{dT}{dt}, \quad (8)$$

where κ represents thermal conductivity, c_p denotes specific heat, and Q_2 denotes heat generated by an internal heat source.

As per the heat conduction equation of the gold film, the gold film absorbs a portion of the laser energy denoted as Q_2 . The interface S_1 experiences convection and thermal radiation, and the thermal boundary conditions can be expressed as follows:

$$-\kappa \frac{\partial T}{\partial \bar{n}} \Big|_{S_1} (t > 0) = h(T - T_0) + \sigma \varepsilon [(T + 273.15)^4 - (T_0 + 273.15)^4], \quad (9)$$

$$Q_2 = \beta I_1 a_2 \exp(-\alpha_2 z), \quad (10)$$

where h is the convective heat transfer coefficient; σ is the Steven-Boltzmann constant, $\sigma = 5.67 \times 10^{-8} \text{ W}/(\text{m}^2 \cdot \text{K}^4)$; β is the energy absorptivity of the mirror; a_2 is the absorption coefficient of the gold film; and ε is the emissivity. The temperature field distribution T_g for the gold film can be obtained by combining Eqs. (8)-(10).

In the heat conduction equation for a monocrystalline silicon substrate, the temperature of the interface S_2 is equal to the temperature at the boundary of the silicon substrate, represented as $T|_{S_2}(t > 0) = T_g$. At the same time, the laser energy irradiated on the substrate becomes exceedingly low and negligible after the laser beam passes through the gold film. In addition, the smaller absorption coefficient of the substrate further reduces the absorption of laser energy. This implies that $Q_2 = 0$. The temperature-field distribution T_s of the monocrystalline silicon substrate can be obtained using Eq. (8).

Owing to the thinness of the gold film, the thermal deformation of the mirror can be considered as a deformation of the substrate. When the temperature field T_s changes unevenly, the thermal strain of the monocrystalline silicon substrate in cylindrical coordinates is expressed by the following thermoelastic equation [26]:

$$\nabla^2 u_r - \frac{u_r}{r^2} + \frac{1}{1-2\mu} \frac{\partial \delta}{\partial r} - \frac{2(1+\mu)}{1-2\mu} \varpi \frac{\partial T_s}{\partial r} = 0, \quad (11)$$

$$\nabla^2 u_z + \frac{1}{1-2\mu} \frac{\partial \delta}{\partial z} - \frac{2(1+\mu)}{1-2\mu} \varpi \frac{\partial T_s}{\partial z} = 0, \quad (12)$$

$$\delta = \frac{\partial u_r}{\partial r} + \frac{u_r}{r} + \frac{\partial u_z}{\partial z}, \quad (13)$$

$$\nabla^2 = \frac{\partial^2}{\partial r^2} + \frac{1}{r} \frac{\partial}{\partial r} + \frac{\partial^2}{\partial z^2}, \quad (14)$$

where u_r and u_z represent the displacement components of the substrate in the r and z directions, respectively; μ is the Poisson's ratio; δ is the volume strain; and ϖ is the thermal expansion coefficient.

It is assumed that the incident angle between the laser beam and mirror is θ . Figure 2 shows the thermal deformation of the mirror at time t . It can be seen that point $A(x, y, z)$ undergoes deformation and moves to the position of point $B(x + \Delta x, y + \Delta y, z + \Delta z)$. This deformation causes a change in the beam propagation path from optical path one to optical path two, resulting in an optical path difference in l . Therefore, the phase difference $\Delta\phi_2$ of the mirror at the coordinate $(x + \Delta x, y + \Delta y)$ can be expressed as follows:

$$\Delta\phi_2 = k \left(-\Delta z + \frac{\Delta y}{\tan \theta} \right). \tag{15}$$

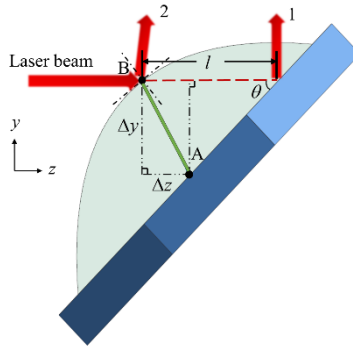


Fig. 2. Thermal deformation of the mirror.

In this study, several laser spot parameters were adopted to analyze the influence of the channel thermal effect on the laser spot distribution, which are given as follows:

(1) Centroid position and mean-squared beam width

The centroid position and mean-squared beam width of the laser spot are defined as follows [27]:

$$\bar{x} = \frac{\int_{-\infty}^{\infty} \int_{-\infty}^{\infty} xI(x, y, z)dx dy}{\int_{-\infty}^{\infty} \int_{-\infty}^{\infty} I(x, y, z)dx dy}, \bar{y} = \frac{\int_{-\infty}^{\infty} \int_{-\infty}^{\infty} yI(x, y, z)dx dy}{\int_{-\infty}^{\infty} \int_{-\infty}^{\infty} I(x, y, z)dx dy}, \tag{16}$$

and

$$w_x^2 = \frac{4 \int_{-\infty}^{\infty} \int_{-\infty}^{\infty} (x - \bar{x})^2 I(x, y, z)dx dy}{\int_{-\infty}^{\infty} \int_{-\infty}^{\infty} I(x, y, z)dx dy}, w_y^2 = \frac{4 \int_{-\infty}^{\infty} \int_{-\infty}^{\infty} (y - \bar{y})^2 I(x, y, z)dx dy}{\int_{-\infty}^{\infty} \int_{-\infty}^{\infty} I(x, y, z)dx dy}, \tag{17}$$

respectively.

(2) Energy Strehl ratio (SR_E)

The energy Strehl ratio is defined as the ratio of the real beam power to the ideal beam power within a given bucket, expressed as follows [28]:

$$SR_E = \frac{\int \int_{x^2+y^2 \leq w^2} I(x, y, z)dx dy}{\int \int_{x^2+y^2 \leq w^2} I_{\text{vacuum}}(x, y, z)dx dy}, \tag{18}$$

where w is the bucket half-width chosen as the mean-squared beam width in vacuum and I_{vacuum} is the intensity in vacuum.

3. Numerical simulation and analysis

Figure 3 shows the complex channel structure. The total length of the channel was 5600 mm, and it comprised several cylindrical pipes with inner and outer diameters of 154 and 160 mm, respectively. Gold-coated monocrystalline silicon mirrors are installed at the corners of the channels. The incident angle between the laser beam and mirror is $\theta = 45^\circ$. The dynamic sealing structure allowed for mutual rotation between the pipes. After the laser propagates within the channel, it enables scanning in both the horizontal and pitch directions. To mitigate the thermal effect of the channel, we propose blowing a purge gas that filters most of the water and dust particles steadily in the positive y direction at the entrance of the channel before laser propagation. It is assumed that the absorption coefficient of the purge gas is significantly lower than that of air, while keeping the other parameters unchanged. The gas turbulence intensity at the channel inlet can be expressed as follows:

$$I_G = 0.16 \times \left(\frac{v_{in} d_{in} \rho_0}{\mu_G} \right)^{-0.125}, \quad (19)$$

where v_{in} denotes the inlet gas velocity, d_{in} represents the hydraulic diameter of the channel inlet, $d_{in} = 154$ mm, and μ_G denotes the gas dynamic viscosity, $\mu_G = 1.7894 \times 10^{-5}$ Pa·s.

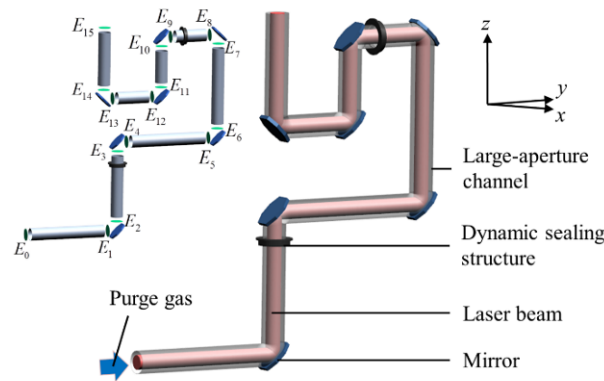


Fig. 3. Complex channel structure of laser propagation.

Previous studies have demonstrated that a scheme for blowing purge gases can effectively create a positive pressure seal in the channel, prevent external environmental contaminants, and ensure a dry and clean environment within the channel [29]. After multiple propagations and reflections of the optical field E_0 at the entrance of the channel, the optical field at the exit section of the channel becomes E_{15} . Using E_{15} as the monitoring target, the influence of the thermal effect of the channel on the laser spot distribution was analyzed. In this study, a multiphase screening method was employed to simulate the phase difference resulting from the gas thermal blooming effect and mirror thermal deformation. Simultaneously, the discrete Fourier transform method was utilized to calculate the beam propagation within the channel. The calculation process is described in detail in [15], and is briefly described here. In the simulation analysis of the fluid domain within the channel, we assumed that the gas was an incompressible fluid with a slightly varying density. The numerical model was subjected to the following boundary conditions. First, the ambient temperature and inlet purge gas temperature are set to 22 °C. Second, the high thermal conductivity of the channel material allows the rapid transfer and dissipation of heat within the channel. Therefore, it was assumed that the temperature of the interface between the channel and gas remained consistently equal to the ambient temperature. Third, in both the no-gas-blowing and gas-blowing schemes, the gas inlet surface of the channel

was defined as the wall surface and velocity inlet, respectively, whereas the outlet surface of the channel always functioned as an outflow boundary. Fourth, the channel had a short length, and the gas absorption coefficient was extremely small. The energy loss during the propagation of the laser beam through the gas medium was neglected, and only the partial energy absorption by the mirror was considered. The basic parameters of the selected numerical simulations are listed in Table 1.

Table 1. Basic parameters of the selected numerical simulations.

Parameter	Symbol	Value
Wavelength (μm)	λ	10.6
Beam waist radius (mm)	ω_0	50
Sound speed (m/s)	c_s	340
Specific heat ratio	γ	1.4
Gas density (kg/m^3)	ρ_0	1.196
Gas refractive index	n_0	1.0002727
Air: absorption coefficient (m^{-1})	α_{1a}	6×10^{-5}
Purge gas: absorption coefficient (m^{-1})	α_{1p}	3×10^{-5}
Mirror: energy absorptivity	β	0.5%
Si: density (kg/m^3)	ρ_s	2330
Si: specific heat ($\text{J}/(\text{kg}\cdot^\circ\text{C})$)	c_{p1}	713.9
Si: thermal conductivity ($\text{W}/(\text{m}\cdot^\circ\text{C})$)	κ_s	140
Si: thermal expansion coefficient ($^\circ\text{C}^{-1}$)	ϖ	2.62×10^{-6}
Si: Poisson's ratio	μ	0.22
Gold: density (kg/m^3)	ρ_g	19320
Gold: absorption coefficient (m^{-1})	α_2	7.65×10^7
Gold: specific heat ($\text{J}/(\text{kg}\cdot^\circ\text{C})$)	c_{p2}	129.81
Gold: thermal conductivity ($\text{W}/(\text{m}\cdot^\circ\text{C})$)	κ_g	297.73

3.1. Effect of propagation time on beam quality

The laser power was selected as $P = 1 \times 10^4 \text{W}$. In the gas-blowing scheme, we set $v_{\text{in}} = 1.6 \text{m/s}$ and $I_G = 0.048 \text{ to}$. Considering the working times of 10 s and 60 s as examples, the temperature distributions of the channel's y - z cross section are shown in Fig. 4 when comparing the schemes with and without gas blowing. As shown in Figs. 4(a) and (b), the gas temperature distribution in the channel is closely correlated with the laser propagation path in a short time. With increasing time, the temperatures of the gas and mirror in the channel increased, and the temperature distribution gradually became disordered. The mirror temperature was higher than that of the gas at various time points. The mirror transmitted heat to the surrounding gas, and the laser beam had an overlapping propagation path in the corner area of the channel; thus, more heat accumulated in the corner area. Comparing Figs. 4(a), (c), and Figs. 4(b) and (d), it can be seen that blowing the purge gas at different times significantly reduced the gas temperature rise in the channel and mitigated the heat accumulation issue. Additionally, it provided forced-convection heat dissipation to the mirror. However, the heat dissipation effect on the mirror is insignificant.

The influence of the channel thermal effect on the beam phase was analyzed from three perspectives: the phase difference resulting from the gas thermal blooming effect, mirror thermal deformation, and the total phase difference of the channel. The phase differences resulting from the channel thermal effect with and without gas blowing are shown in Figs. 5 and 6, respectively. Figure 5 shows that the phase differences resulting from the gas thermal blooming effect and

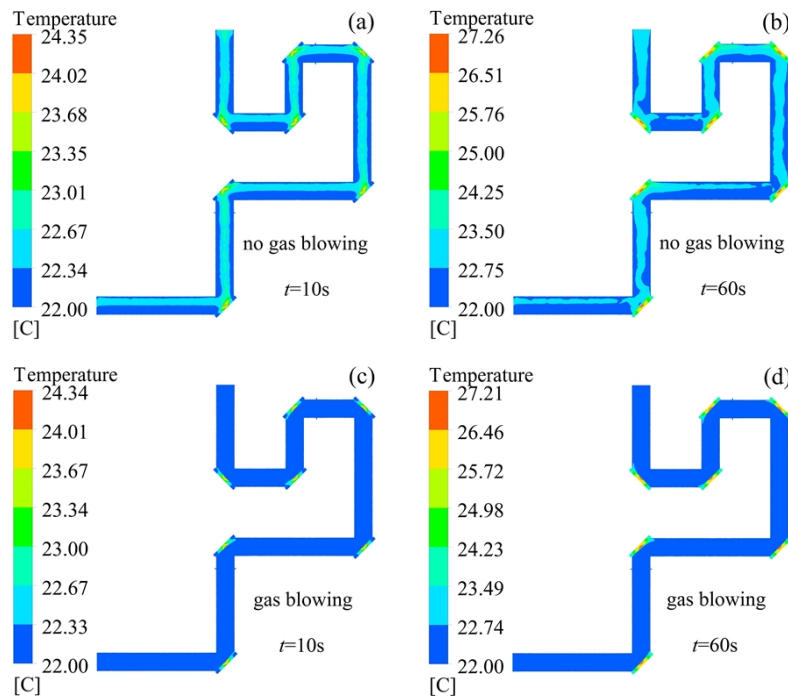


Fig. 4. Temperature distributions of the channel's y - z cross section for different working conditions and time when $P = 1 \times 10^4 \text{W}$. (a), (b) no gas blowing; (c), (d) gas blowing. (a), (c) $t = 10 \text{ s}$; (b), (d) $t = 60 \text{ s}$.

mirror thermal deformation are similar to a Gaussian distribution at different times. Although they can cancel each other owing to their opposite effects on the beam phase, the presence of this nonuniform compensation causes a significant distortion of the beam phase. The total phase difference of the channel exhibited significant variation in the y direction and demonstrated a certain degree of symmetry in the x direction. As time increases, the phase difference caused by the gas thermal blooming effect changes more significantly than the thermal deformation of the mirror, resulting in a more pronounced effect on the beam phase. As shown in Fig. 6, owing to the gas turbulence effect and discharge of hot gas, the phase difference caused by the gas thermal blooming effect no longer follows the characteristics of a Gaussian distribution. At different times, the total phase difference of the channel closely resembled the phase difference caused by the mirror thermal deformation. This indicates that mirror thermal deformation is the primary factor affecting the beam phase after the purge gas is blown. By comparing Figs. 5 and 6, it can be observed that blowing the purge gas can effectively alleviate the phase difference caused by the gas thermal blooming effect in the channel at different times. This mitigation effect became more pronounced with time. However, their ability to mitigate the phase difference in the thermal deformation of mirrors is limited.

Within 60-s of laser propagation, the change in the laser spot parameters at the monitoring target (E_{15}) with time was analyzed. The variation curves of the laser spot centroid position \bar{x} and \bar{y} with time t under both the no-gas-blowing and gas-blowing conditions are shown in Fig. 7. Figure 7(a) shows that \bar{x} was in a fluctuating state when no gas was blown. After blowing the gas, the offset of \bar{x} was significantly reduced, and the change remained relatively stable. Figure 7(b) shows that the offset of \bar{y} is larger in the absence of gas blowing, and the offset along the $-y$ direction becomes more pronounced over time. After blowing the gas, the offset

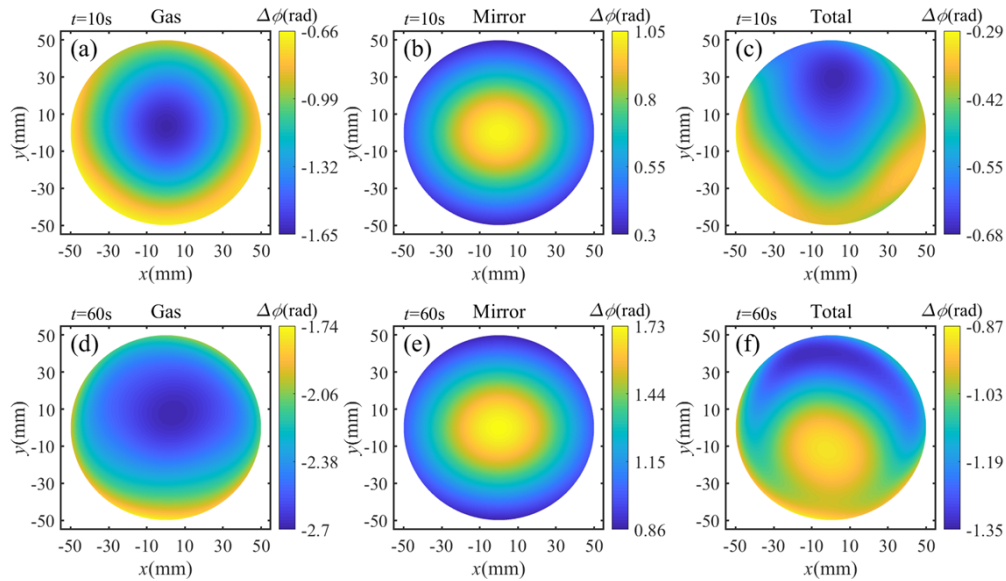


Fig. 5. Phase differences resulting from the gas thermal blooming effect and mirror thermal deformation at different times with no gas blowing and total phase difference of the channel. (a), (d) Gas; (b), (e) Mirror; (c), (f) Total. (a), (b), (c) $t = 10$ s; (d), (e), (f) $t = 60$ s.

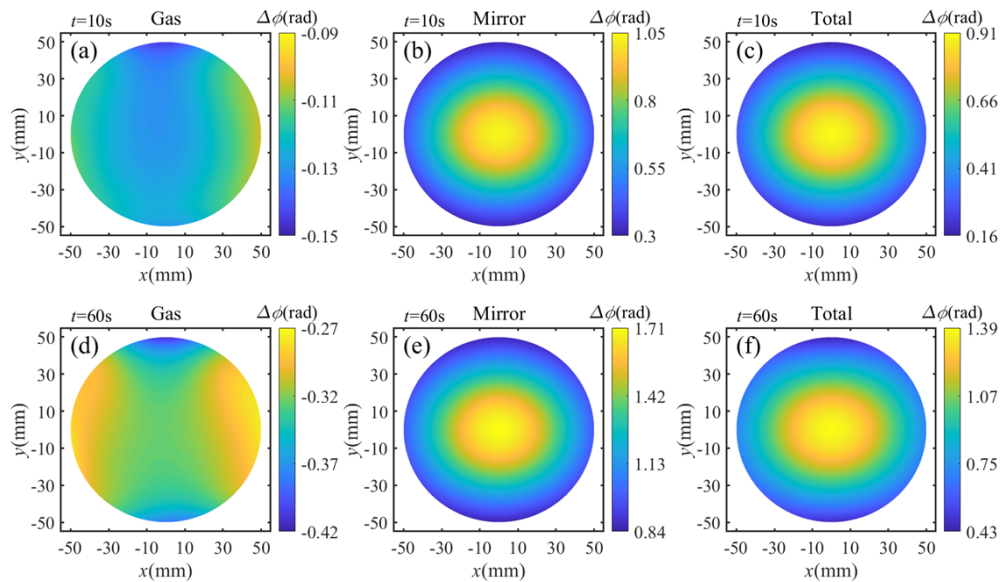


Fig. 6. Phase differences resulting from the gas thermal blooming effect and mirror thermal deformation at different times with gas blowing and total phase difference of the channel. (a), (d) Gas; (b), (e) Mirror; (c), (f) Total. (a), (b), (c) $t = 10$ s; (d), (e), (f) $t = 60$ s.

of \bar{y} in the $-y$ direction decreased significantly and remained stable. It has been proven that, at different times, the channel thermal effect without gas blowing causes the laser spot centroid position to shift significantly. Selecting a gas-blowing scheme can effectively reduce the centroid shift and alleviate centroid jitter. A comparison of Figs. 7(a) and (b) shows that the offset of the beam centroid \bar{y} is larger than that of \bar{x} at different times. The reason is that the channel is symmetrical along the x -axis. Without blowing gas, the hot gas in the channel rises along the z -axis, which aggravates the difference in gas density along the z -axis. After blowing the gas, owing to the influence of the flow field distribution in the channel, the distribution of the flowing hot gas along the y - or z -axis within the channel is uneven but along the x -axis is approximately symmetrical. Consequently, there is a significant difference in gas density along the y - or z -axis of the channel cross-section. In summary, after the coordinate transformation of laser propagation, the difference in gas density with and without gas blowing always makes the laser spot at the exit section of the channel change more obviously along the y -axis. This observation provides evidence that the thermal effect of the channel has a more significant influence on the centroid position of the laser spot in the y direction. Meanwhile, the difference in gas density continues to increase with time, making the offset of \bar{y} more pronounced over time.

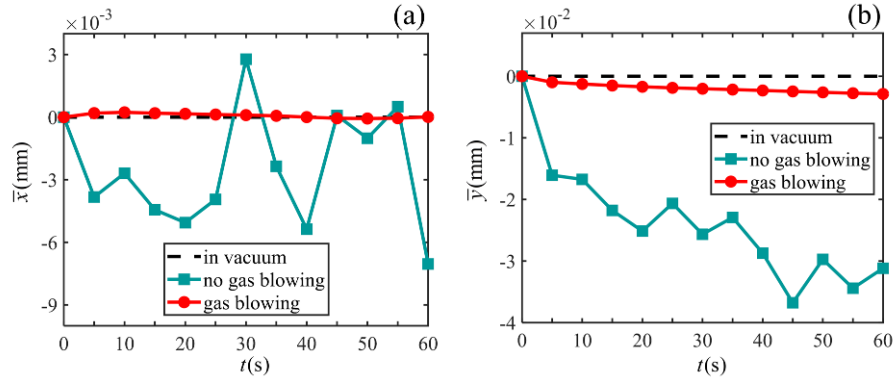


Fig. 7. Variation curves of the laser spot centroid positions \bar{x} and \bar{y} with time t with and without no gas blowing when $P = 1 \times 10^4$ W. (a) \bar{x} ; (b) \bar{y} .

The variation curves of the laser spot mean-squared beam width w_x and w_y and astigmatism parameter w_x/w_y with time t under both no-gas-blowing and gas-blowing conditions are shown in Fig. 8. The astigmatism parameter w_x/w_y represents beam symmetry; the closer the w_x/w_y is to one, the better the laser spot symmetry. Figures 8(a) and (b) show that the mean-squared beam widths w_x and w_y decreased in a short time and then increased rapidly in the absence of gas blowing. These values are higher than the ideal value in the vacuum state and exhibit a gradual upward trend. After blowing the gas, both w_x and w_y gradually decreased over time and eventually stabilized. At different times, the values of w_x and w_y during gas blowing were consistently smaller than those without gas blowing and in vacuum. It was proven that the channel thermal effect without gas blowing causes the laser spot to diverge significantly. Gas blowing effectively mitigated the divergence of the laser spot and enhanced its stability. Figure 8(c) shows that w_x/w_y is consistently greater than one for both no gas blowing and gas blowing, indicating a similar distortion of the laser spot shape at different times. Without blowing gas, w_x/w_y increased rapidly with time, reached its peak at approximately 30 s, and then decreased rapidly. It was demonstrated that the change in the shape of the laser spot was fast and irregular. During gas blowing, w_x/w_y approaches the ideal vacuum state, and its value steadily increases to a stable value over time. This finding provides evidence that the gas-blowing scheme effectively mitigates the laser spot distortion, enhances the symmetry of the laser spot distribution, and promotes

a more stable change in the laser spot shape. The variation curves of the energy Strehl ratio SR_E with time t under both the no-gas-blowing and gas-blowing conditions are shown in Fig. 9. Without gas blowing, SR_E exhibits a rapid increase, followed by a sharp decrease to a value of less than one. It has been proven that the channel thermal effect without gas blowing causes a divergence in the energy of the laser spot. After gas blowing, SR_E gradually stabilizes at a value greater than one. This is because the mirror thermal deformation is the primary factor affecting the beam phase after the purge gas is blown, and the phase difference caused by the mirror thermal deformation leads to the energy concentration of the laser spot.

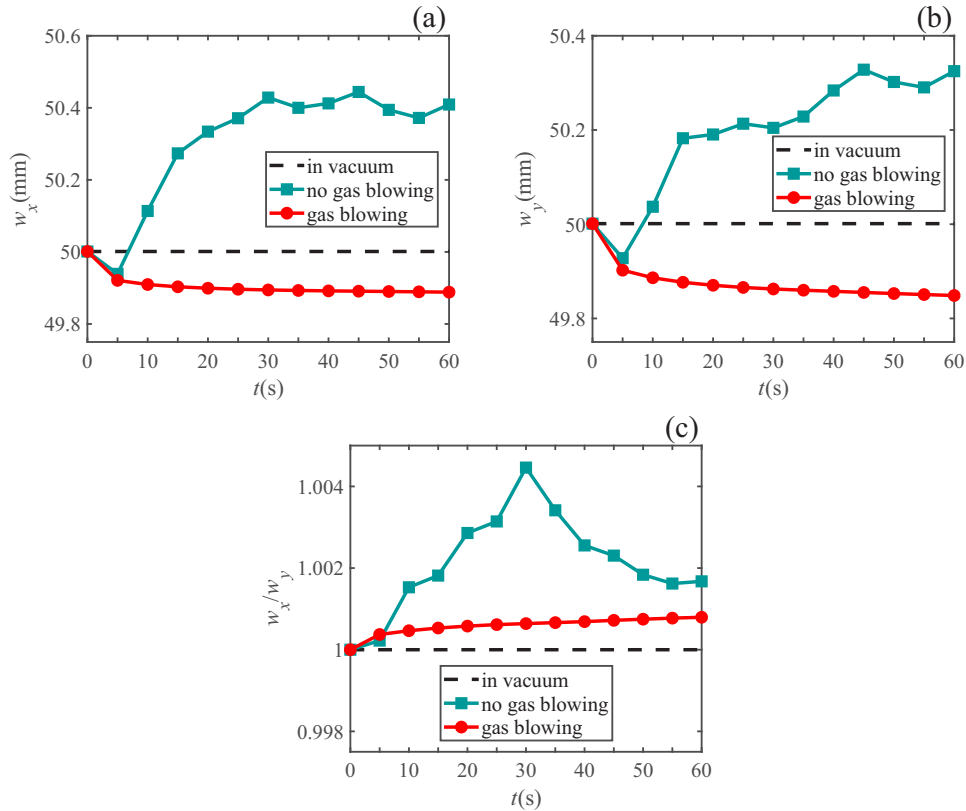


Fig. 8. Variation curves of the laser spot mean-squared beam width w_x and w_y and astigmatism parameter w_x/w_y with time t under both no gas blowing and gas blowing conditions with $P = 1 \times 10^4$ W. (a) w_x ; (b) w_y ; (c) w_x/w_y .

3.2. Effect of laser power on beam quality

The laser power was selected as $P = 1 \times 10^3$ W and the gas-blowing scheme is the same as that described in Section 3.1. Considering a working time of 10 s as an example, the temperature distributions of the channel's y - z cross section of the channel are shown in Fig. 10 when comparing the schemes with and without gas blowing. Figures 10(a) and 4(a) show that as the laser power decreases, there is a corresponding reduction in heat accumulation within the channel. This decrease in laser power also leads to a lower temperature rise in both the gas and mirror. Comparing Figs. 10(b) and 4(c), it is evident that the gas-blowing scheme enables the channel to efficiently discharge the hot gas. As a result, variations in the laser power primarily affected the temperature increase of the mirror, whereas the gas temperature remained relatively stable.

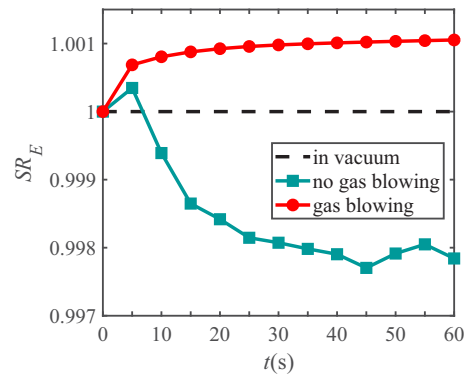


Fig. 9. Variation curves of the energy Strehl ratio SR_E with time t under both no gas blowing and gas blowing conditions with $P = 1 \times 10^4 \text{W}$.

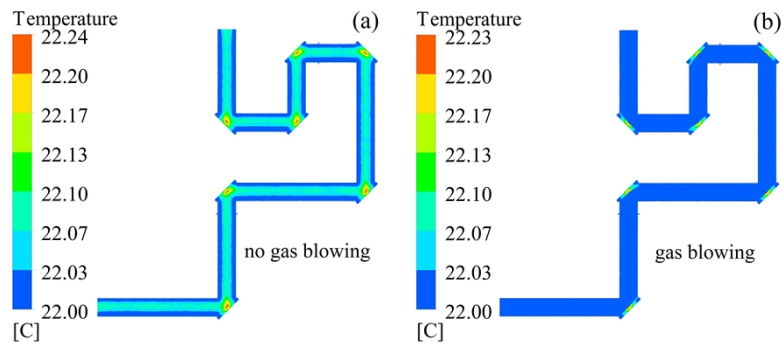


Fig. 10. Temperature distributions of the channel's y-z cross section for different working conditions when $P = 1 \times 10^3 \text{W}$ and $t = 10 \text{s}$. (a) no gas blowing; (b) gas blowing.

Considering the laser propagation for 60 s as an example, the phase differences resulting from the channel thermal effect are shown in Fig. 11 when comparing the schemes of the no gas blowing and gas blowing conditions. Figures 11(a) and (b) show the phase differences generated by the gas thermal blooming effect and mirror thermal deformation still follow a Gaussian distribution at a low laser power. Furthermore, the nonuniform compensation of these phase differences results in a beam phase offset. On comparing Figs. 11(a) and (b) with Figs. 5(d) and (e), it is evident that the gas thermal blooming effect under different laser powers remains the primary factor affecting the beam phase in the no-gas-blowing scheme. With increasing laser power, the phase difference caused by the gas thermal blooming effect underwent greater changes, resulting in a higher impact on the beam phase. Comparing Figs. 11(d) and (e) with Figs. 6(d) and (e), it can be seen that gas blowing can significantly reduce the phase difference caused by the gas thermal blooming effect at different laser powers, while having a minimal impact on the phase difference caused by the mirror thermal deformation. Additionally, the primary cause of the channel thermal effect was the thermal deformation of the mirror.

The change in the laser spot parameters at the monitoring target (E_{15}) with laser power was analyzed. The variation curves of the laser spot centroid positions \bar{x} and \bar{y} with laser power P under both the no gas blowing and gas blowing conditions are shown in Fig. 12. Figure 12(a) shows that the offset of \bar{x} fluctuates as the laser power increases in the absence of gas blowing, and the amplitude of the change increases gradually. After blowing the gas, the offset of \bar{x} was significantly reduced, and the change remained relatively stable. Figure 12(b) shows that the

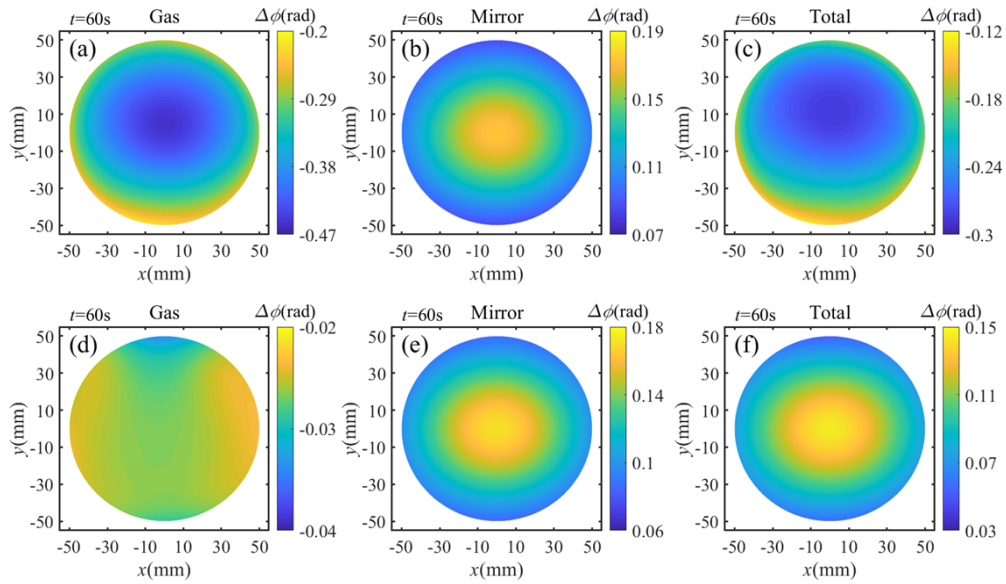


Fig. 11. Phase differences resulting from the gas thermal blooming effect and mirror thermal deformation with $P = 1 \times 10^3$ W and $t = 60$ s under the conditions of no gas blowing and gas blowing and the total phase difference of the channel. (a), (d) Gas; (b), (e) Mirror; (c), (f) Total. (a), (b), (c) no gas blowing; (d), (e), (f) gas blowing.

offset of \bar{y} in the $-y$ direction is significant in the absence of gas blowing, and the offset increases gradually with the increase in power. After blowing the gas, the offset of \bar{y} was significantly reduced, and the offset change exhibited higher stability. It was proven that the channel thermal effect in the absence of gas blowing causes the laser spot centroid to shift significantly at different laser powers. Gas blowing can effectively reduce the centroid shift and alleviate centroid jitter. Comparing Figs. 12(a) and (b), it can be observed that the offset of the beam-centroid \bar{y} is also higher than that of \bar{x} at different powers.

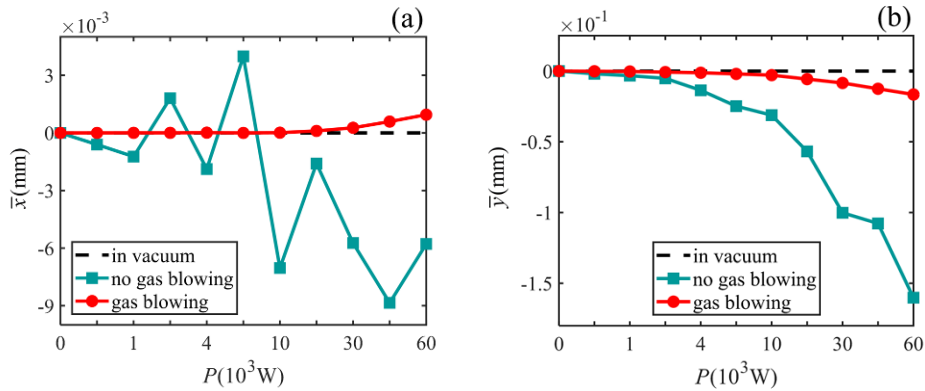


Fig. 12. Variation curves of the laser spot centroid positions \bar{x} and \bar{y} with power P under both no gas blowing and gas blowing conditions at $t = 60$ s. (a) \bar{x} ; (b) \bar{y} .

The variation curves of the laser spot mean-squared beam width w_x and w_y and astigmatism parameter w_x/w_y with laser power P under both the no gas blowing and gas blowing conditions are shown in Fig. 13. Figures 13(a) and (b) illustrate that w_x and w_y gradually increase with P in

the absence of gas blowing. The reason is that the gas thermal blooming effect is the primary factor affecting the beam phase in the absence of gas blowing, and this influence becomes more obvious with increasing power. The phase difference caused by the gas thermal blooming effect causes the laser spot to diverge significantly. When gas is blown, w_x and w_y gradually decrease with an increase in P , which is the opposite of the change pattern without gas blowing. This is because the mirror thermal deformation is the primary factor affecting the beam phase after the purge gas is blown, and the degree of influence continues to increase with increasing power. The phase difference caused by the mirror thermal deformation leads to the energy concentration of the laser spot. At different powers, the values of w_x and w_y were consistently smaller when gas blowing was applied compared to the cases of no gas blowing and vacuum. This provided evidence that the gas-blowing scheme was effective in reducing the mean-square beam width of the laser spot, suppressing the divergence of the laser spot and enhancing the stability of the laser spot shape. Figure 13(c) shows that w_x/w_y is consistently greater than one with and without gas blowing. The reason for the change is that the difference in laser spot at the exit section of the channel along the y -axis direction is more obvious with and without gas blowing. Therefore, the distortion of the laser spot in the y direction is more serious, so that w_y is less than w_x . Meanwhile, the difference in laser spot along the y -axis increases gradually with the increase in laser power, so that w_x/w_y shows a gradual increase with increasing laser power. However, at different powers, the w_x/w_y tends to be closer to the vacuum state when gas blowing is applied. This finding provides evidence that despite the laser spot distortion becoming more pronounced with increasing laser power, the gas-blowing scheme improved the symmetry of the laser spot compared to the no-gas-blowing scheme. The variation curves of the energy Strehl ratio SR_E with power P under both the no-gas-blowing and gas-blowing conditions are shown in Fig. 14. It can be observed that the value of SR_E gradually decreases with increasing P when there is no gas blowing. By contrast, the changing trend of SR_E in the gas-blowing scheme is completely the opposite, and it is always greater than one. This demonstrates that the gas-blowing scheme effectively enhanced the energy concentration of the laser spot at different laser powers. Furthermore, this enhancement effect became more pronounced as the laser power increased.

3.3. Effect of inlet gas velocity on beam quality

The laser power was selected as $P = 1 \times 10^4 \text{W}$. Considering a working time of 60 s as an example, the temperature distributions of the channel's y - z cross section is shown in Fig. 15 when v_{in} is 0.4 m/s and 2 m/s. A comparison of Figs. 15(a) and (b) shows that a larger inlet gas velocity has a more pronounced impact on mitigating the heat accumulation at the corner of the channel. However, variations in the gas velocity do not significantly influence the temperature rise of either the gas or the mirror. At different inlet gas velocities, the mirror temperature consistently exceeded the gas temperature, and increasing the gas velocity was more effective in reducing the temperature increase of the mirror. Figure 16 shows the phase differences resulting from channel thermal effects at different inlet gas velocities. By comparing the phase difference at different v_{in} , it becomes evident that the change in gas velocity primarily impacts the phase difference resulting from the gas thermal blooming effect, while having a minimal effect on the phase difference resulting from mirror thermal deformation. Despite the varying levels of turbulence effects in the gas owing to different gas velocities, the total phase difference remains similar to the phase difference resulting from mirror thermal deformation. It is proven that the phase difference caused by the mirror thermal deformation remains the most significant factor influencing the beam phase. Furthermore, the influence of mirror thermal deformation on the beam phase increased with higher gas velocities.

Considering the laser propagation for 60 s as an example, the change in the laser spot parameters at the monitoring target (E_{15}) with the inlet gas velocity was analyzed. The value range of v_{in} was set to 0.2-2 m/s, and the turbulence intensity I_G for different gas velocities was obtained

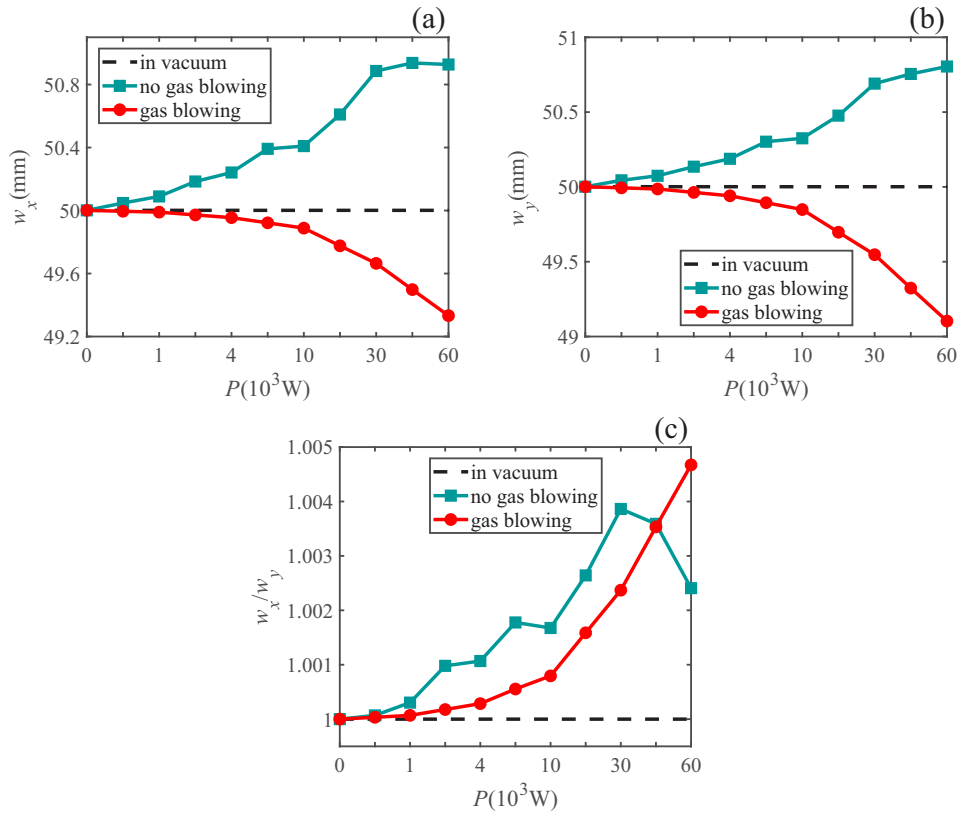


Fig. 13. Variation curves of the laser spot mean-squared beam width w_x and w_y and astigmatism parameter w_x/w_y with power P under both the no gas blowing and gas blowing conditions at $t = 60$ s. (a) w_x ; (b) w_y ; (c) w_x/w_y .

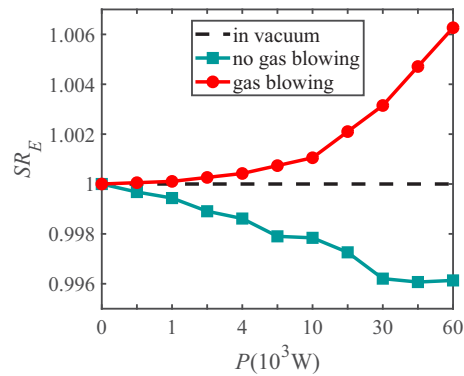


Fig. 14. Variation curves of the energy Strehl ratio SR_E with power P under both the no gas blowing and gas blowing conditions at $t = 60$ s.

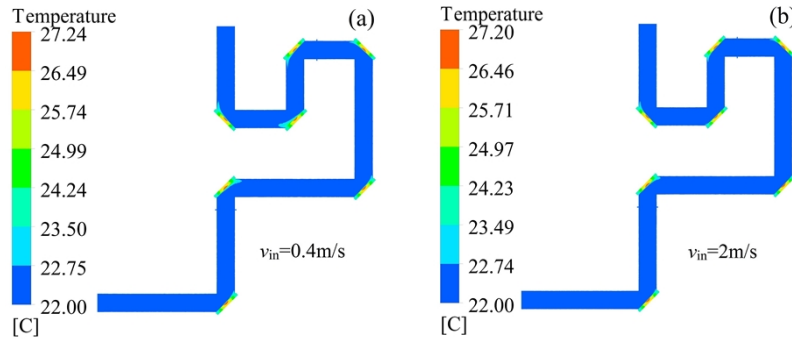


Fig. 15. Temperature distributions of the channel's y - z cross section for different inlet gas velocities with $P = 1 \times 10^4 \text{ W}$ and $t = 60 \text{ s}$. (a) $v_{\text{in}} = 0.4 \text{ m/s}$; (b) $v_{\text{in}} = 2 \text{ m/s}$.

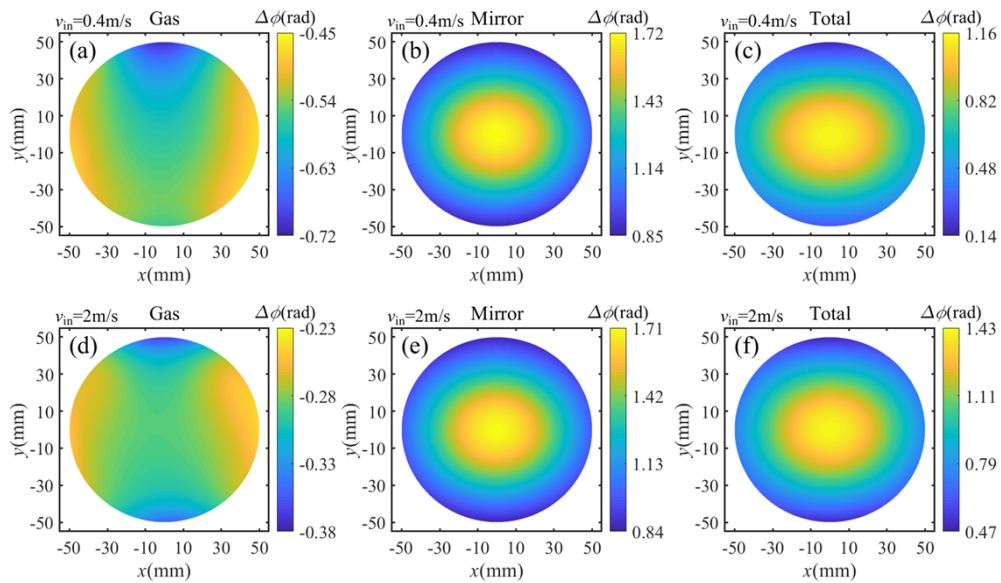


Fig. 16. Phase differences caused by the gas and the mirror and the total phase difference of the channel at different inlet gas velocities with $P = 1 \times 10^4 \text{ W}$ and $t = 60 \text{ s}$. (a), (d) Gas; (b), (e) Mirror; (c), (f) Total. (a), (b), (c) $v_{\text{in}} = 0.4 \text{ m/s}$; (d), (e), (f) $v_{\text{in}} = 2 \text{ m/s}$.

using Eq. (19). The variation curves of the laser spot centroid positions \bar{x} and \bar{y} with gas velocity v_{in} are shown in Fig. 17. It can be observed that \bar{x} and \bar{y} gradually approach the ideal values expected in a vacuum as v_{in} increases. This finding confirms that the ability to alleviate the offset of the laser spot centroid increased with the increase in gas velocity. The variation curves of the laser spot mean-squared beam width w_x and w_y with gas velocity v_{in} are shown in Fig. 18. As v_{in} increases from zero, both w_x and w_y exhibit a sharp initial decrease, followed by slower changes; however, they consistently remain smaller than the ideal vacuum value. When $v_{in} > 0.8$ m/s, w_x and w_y show only slight changes. Gas blowing has been proven to have a consistent effect on the mean-square beam width of a laser spot in different directions. Furthermore, when the gas velocity reached a certain value, the mean-squared beam width reached a stable state. The variation curves of the astigmatism parameter w_x/w_y and energy Strehl ratio SR_E with respect to the gas velocity v_{in} are shown in Fig. 19. As v_{in} increased from zero, w_x/w_y exhibited an abrupt decrease, whereas SR_E showed an abrupt increase. Subsequently, both w_x/w_y and SR_E changed gradually with an increase in the gas velocity, consistently remaining greater than one. When $v_{in} > 0.8$ m/s, the changes in w_x/w_y and SR_E were less pronounced. Gas blowing has been proven to effectively correct the distortion of the laser spot and enhance its symmetry and energy concentration. An appropriate increase in the gas velocity is beneficial for improving the laser spot quality. However, once the gas velocity exceeded a certain threshold, the shape and energy distribution of the laser spot tended to stabilize.

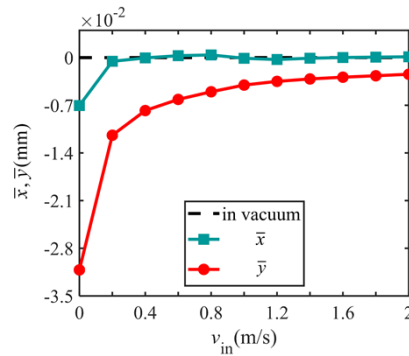


Fig. 17. Variation curves of the laser spot centroid positions \bar{x} and \bar{y} with gas velocity v_{in} with $P = 1 \times 10^4$ W and $t = 60$ s.

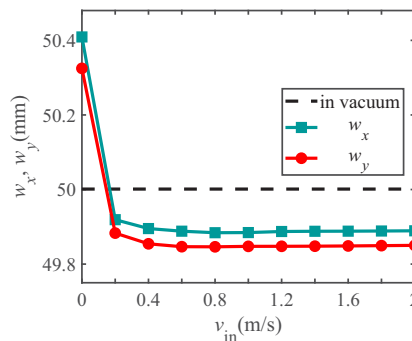


Fig. 18. Variation curves of the laser spot mean-squared beam width w_x and w_y with gas velocity v_{in} with $P = 1 \times 10^4$ W and $t = 60$ s.

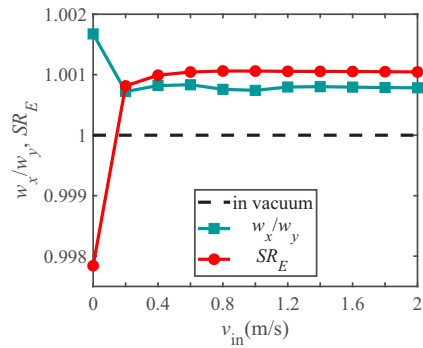


Fig. 19. Variation curves of the astigmatism parameter w_x/w_y and energy Strehl ratio SR_E with gas velocity v_{in} with $P = 1 \times 10^4$ W and $t = 60$ s.

4. Experimental verification

The thermal effect on the channel became more pronounced as the laser power increased. However, the measurement of the beam phase of high-power lasers is a complex and challenging task. To validate the accuracy of the model-establishment approach, we reduced the laser power and simplified the channel structure. By establishing a numerical model that replicates the simplified experiment, we compared the phase-detection results obtained from both the simulation and experiment. Figure 20 shows the beam phase detection experiment after the laser beam propagates through the glass pipe. The experimental investigation includes the following contents. First, the analysis focuses on the influence of the gas thermal blooming effect in the glass tube on the beam phase in the absence of nitrogen blowing. Second, the effect of nitrogen blowing on alleviating the gas thermal blooming effect in the channel was examined. In the experiment, the laser wavelength was $\lambda = 9.3 \mu\text{m}$ and the output power of the laser was uniformly adjusted using a signal generator. The laser beam was expanded and collimated through a beam expander-collimator system, resulting in an approximately parallel beam with a beam waist radius of $\omega_0 = 7.5$ mm. The glass pipe used in the experiment was cylindrical with an inner diameter of 20 mm, outer diameter of 26 mm, and length of 2000 mm. One end of the pipe was sealed with a ZnSe planar lens, and the nitrogen inlet was opened. The hydraulic diameter of the nitrogen inlet was $d_{in} = 6$ mm and the nitrogen velocity is $v_{in} = 10$ m/s. The other end of the pipe serves as a free outlet. After the laser beam passes through the beam splitter and attenuator, the phase change is detected using a wavefront sensor.

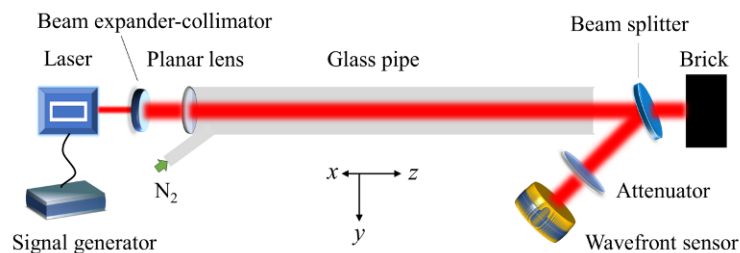


Fig. 20. Beam phase detection experiment after a laser beam propagates through the glass pipe.

Experimental measurements were conducted to determine the beam phase difference after the laser propagated for 60 s, both with and without gas blowing at powers of 5 W and 20 W. Figure 21 presents the simulation data and experimental results of the phase difference

distribution for different laser powers under both the no gas blowing and gas blowing conditions at $t = 60$ s. Comparing Figs. 21(a1), (a2), (b1), and (b2), it is evident that both the simulation and experimental results exhibit characteristics similar to a Gaussian distribution under the no-gas-blowing scheme for different laser powers. It is challenging to eliminate errors during the experimental measurement process, and there may be some fluctuations in the experimental results. Nevertheless, the phase difference distribution characteristics observed in both the simulation and experiment remain largely consistent. By comparing Figs. 21(c1), (c2), (d1), and (d2), it can be seen that the phase difference distribution in both the simulation and experimental results under the gas-blowing scheme and at different laser powers exhibits a certain symmetry in the x direction. Additionally, owing to the uneven hot-gas discharge caused by the angle of the gas direction at the inlet, the phase difference experiences an offset in the same direction along the y -axis. However, there were some differences in the offset values due to experimental errors. In summary, the phase difference distribution characteristics obtained from both the numerical simulation and experimental results exhibited significant similarities under both the no-gas-blowing and gas-blowing conditions. This provides evidence of the accuracy of the numerical model.

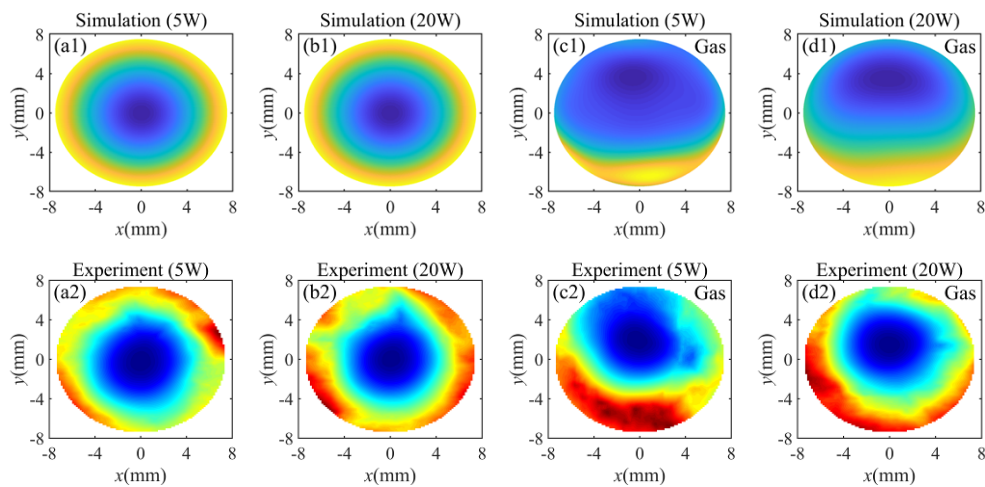


Fig. 21. Simulation data and experimental results of the phase difference distribution for different laser powers under both no gas blowing and gas blowing conditions at $t = 60$ s. (a1), (b1), (c1), (d1) Simulation; (a2), (b2), (c2), (d2) Experiment. (a1), (a2), (b1), (b2) no gas blowing; (c1), (c2), (d1), (d2) gas blowing. (a1), (a2), (c1), (c2) 5 W; (b1), (b2), (d1), (d2) 20 W.

5. Conclusion

In this study, a numerical model was developed to describe the thermal effects of high-power laser propagation in complex channels. The influence of the channel thermal effect on the beam phase and laser spot as the laser propagation time and power varied was analyzed and compared in detail under both the no-purge gas blowing and purge gas blowing schemes. The numerical analysis results indicated that as the laser propagation time and power increased, significant heat accumulation occurred in the channel under the no-gas-blowing scheme. The gas thermal blooming effect has a more pronounced effect on the beam phase than the mirror thermal deformation. However, their influence on the beam phase is essentially the opposite, and this non-uniform compensation causes a significant distortion and offset of the beam phase. The centroid position of the laser spot exhibits significant jitter and offset. The offset of the

centroid position \bar{y} along the $-y$ direction is more evident. The mean-squared beam widths w_x and w_y of the laser spot increased unevenly. Therefore, the distortion and divergence of the laser spot are significant, which further changes the energy Strehl ratio SR_E by less than one. When the gas-blowing scheme was implemented, the gas thermal blooming effect in the channel was significantly alleviated. Consequently, the main influence on the beam phase was from the thermal deformation of the mirror. Despite the introduction of gas turbulence, the centroid position offset was reduced by several orders of magnitude. Simultaneously, both w_x and w_y decreased uniformly, whereas SR_E remained greater than one. Additionally, w_x/w_y approached the ideal vacuum value and the change remained stable. These changes provide evidence that the gas-blowing scheme significantly improves the symmetry, stability, and energy concentration of the laser spot. Increasing the inlet gas velocity was advantageous for mitigating the channel thermal effect. However, it is worth noting that once the gas velocity exceeds 0.8 m/s, the laser spot parameters will no longer change significantly. Finally, an experimental platform for the simplified channel was constructed. By comparing the experimental and simulation results, it was observed that the distribution characteristics of the beam phase differences were similar. This similarity provides evidence of the accuracy of the numerical model.

Funding. State Key Laboratory of Laser Interaction with Matter (E12701SZCZ00).

Disclosures. The authors declare no conflicts of interest.

Data availability. The data underlying the results presented in this paper are not publicly available at this time but may be obtained from the authors upon reasonable request.

References

1. J. R. Cook, "High-energy laser weapons since the early 1960s," *Opt. Eng.* **52**(2), 021007 (2012).
2. A. Exrance, "Military technology: Laser weapons get real," *Nature* **521**(7553), 408–410 (2015).
3. J. Zuo and X. Lin, "High-power laser systems," *Laser Photonics Rev.* **16**(5), 2100741 (2022).
4. P. Sprangle, A. Ting, J. Penano, *et al.*, "Incoherent combining and atmospheric propagation of high-power fiber lasers for directed-energy applications," *IEEE J. Quantum Electron.* **45**(2), 138–148 (2009).
5. R. Fischer, A. Ting, G. DiComo, *et al.*, "Absorption and scattering of 1.06 microm laser radiation from oceanic aerosols," *Appl. Opt.* **48**(36), 6990–6999 (2009).
6. G. Chen and C. Wang, "Modeling of laser heating GaAs considering the effects of atmospheric thermal blooming with crosswind," *Optik* **131**, 11–20 (2017).
7. F. Gebhardt and D. Smith, "Self-induced thermal distortion in the near field for a laser beam in a moving medium," *IEEE J. Quantum Electron.* **7**(2), 63–73 (1971).
8. F. G. Gebhardt, "Twenty-five years of thermal blooming: an overview," *Proc. SPIE* **1221**, 2–25 (1990).
9. J. A. Fleck, J. R. Morris, and M. D. Feit, "Time-dependent propagation of high energy laser beams through the atmosphere," *Appl. Phys.* **10**(2), 129–160 (1976).
10. J. A. Fleck, J. R. Morris, and M. D. Feit, "Time-dependent propagation of high energy laser beams through the atmosphere: II," *Appl. Phys.* **14**(1), 99–115 (1977).
11. X. Li and X. Ji, "Effect of thermal blooming on the beam quality of truncated laser beams," *Optik* **127**(20), 8350–8356 (2016).
12. X. Ji, Y. Baykal, and X. Jia, "Changes of the centroid position of laser beams propagating through an optical system in turbulent atmosphere," *Opt. Laser Technol.* **54**, 199–207 (2013).
13. X. Ji, H. T. Eyyuboğlu, G. Ji, *et al.*, "Propagation of an Airy beam through the atmosphere," *Opt. Express* **21**(2), 2154–2164 (2013).
14. Z. Ding, X. Li, J. Cao, *et al.*, "Thermal blooming effect of Hermite–Gaussian beams propagating through the atmosphere," *J. Opt. Soc. Am. A* **36**(7), 1152–1160 (2019).
15. L. Zhao, J. Wang, M. Guo, *et al.*, "Steady-state thermal blooming effect of vortex beam propagation through the atmosphere," *Opt. Laser Technol.* **139**, 106982 (2021).
16. X. Li, J. Cao, Z. Ding, *et al.*, "Influence of fill factors on the thermal blooming of array laser beams in the air," *Optik* **182**, 314–323 (2019).
17. Y. Zhang, T. Hou, H. Chang, *et al.*, "Thermal blooming effect and the scaling laws of partial spatially coherent beam array propagating through the atmosphere," *Results Phys.* **26**, 104444 (2021).
18. L. Wang, W. Lin, C. Wu, *et al.*, "The steady-state thermal blooming of the high-power laser propagation in the rain," *J. Electromagn. Waves Appl.* **30**(14), 1877–1884 (2016).
19. L. Wang and W. Lin, "The effect of the wind speed on the thermal blooming of a laser beam propagating in the rain," *J. Russ. Laser Res.* **38**(5), 455–458 (2017).
20. Y. Zhang, X. Ji, X. Li, *et al.*, "Thermal blooming effect of laser beams propagating through seawater," *Opt. Express* **25**(6), 5861–5875 (2017).

21. L. Lu, Z. Wang, P. Zhang, *et al.*, “Thermal blooming induced phase change and its compensation of a Gaussian beam propagation in an absorbing medium,” *Opt. Lett.* **46**(17), 4304–4307 (2021).
22. M. F. Spencer, “Wave-optics investigation of turbulence thermal blooming interaction: I. Using steady-state simulations,” *Opt. Eng.* **59**(8), 081804 (2020).
23. M. F. Spencer, “Wave-optics investigation of turbulence thermal blooming interaction: II. Using time-dependent simulations,” *Opt. Eng.* **59**(8), 081805 (2020).
24. J. W. Strohbehn, *Laser Beam Propagation in the Atmosphere* (Springer-Verlag, New York, 1978).
25. A. Hussein, L. Hao, C. Yan, *et al.*, “Finite element simulation of the temperature and stress fields in single layers built without-support in selective laser melting,” *Mater. Des.* **52**, 638–647 (2013).
26. W. Nowacki, *Thermoelasticity* (Elsevier, Amsterdam, The Netherlands, 2013), pp. 161–173.
27. H. Weber, “Propagation of higher-order intensity moments in quadratic-index media,” *Opt. Quant. Electron.* **24**(9), S1027–S1049 (1992).
28. Y. H. Yan, B. Q. Liu, B. Zhou, *et al.*, “Studies of energy Strehl ratio of a collimated Gaussian beam in turbulent atmosphere,” *Proc. SPIE* **8906**, 89062H1 (2013).
29. X. Huang, Y. Wu, Y. Shi, *et al.*, “Aerodynamic window sealing of a large-aperture channel for high-power laser transmission,” *Appl. Sci.* **12**(14), 7301 (2022).